ACS APPLIED MATERIALS & INTERFACES

www.acsami.org

Research Article

# Root-Nodule-Inspired Cobalt Selenide with Sulfur-Doping-Induced Phase Transition for High-Performance Lithium−Sulfur Batteries

Wei Yan,[#] Jun Chen,[#] Abdul Mateen,[#] Lin bin Tang, Jiawen Li, Guoxiang Chen, Yongfeng Mei, and Zhihao Bao*

Cite This: *ACS Appl. Mater. Interfaces* 2026, 18, 4779−4791

Read Online

ACCESS | Metrics & More | Article Recommendations | Supporting Information

**ABSTRACT:** The root-nodule system in legumes enables efficient biological nitrogen fixation through symbiotic interactions and hierarchical mass transport. Inspired by this natural architecture, we synthesized a cobalt selenide (CoSe) catalyst supported on carbon nanofibers (CoSe@C) that mimics this root-nodule structure. This unique design promotes rapid electron transport and facilitates efficient catalytic conversion of lithium polysulfides (LiPSs) to $Li_2S$. Through controlled sulfur doping, the initial hexagonal phase of CoSe (h-CoSe) underwent a phase transition to an orthorhombic structure (o-CoSeS), which exhibited a high-spin state due to an increased density of unpaired electrons in the Co d-orbitals. Density functional theory (DFT) calculations revealed that this electronic configuration enhances orbital hybridization between Co d-orbitals and LiPSs p-orbitals, thereby strengthening LiPS adsorption and accelerating the redox kinetics. When o-CoSeS supported on carbon nanofibers (o-CoSeS@C) was used to modify the separator in lithium−sulfur (Li−S) batteries, the battery delivered an initial discharge capacity of 1509 mAh $g^{-1}$ at 0.1 C and maintained an ultralow decay rate of 0.057% per cycle over 1000 cycles at 1 C. The exceptional cycling stability stems from the synergy between the biomimetic hierarchical network, which facilitates mass/charge transport, and the optimized electronic structure of the Co active sites, which boosts catalytic activity. This work proposes a novel biomimetic strategy for designing high-performance catalysts for Li−S batteries and provides atomic-level insights into the regulation of transition-metal electronic states for catalytic optimization.

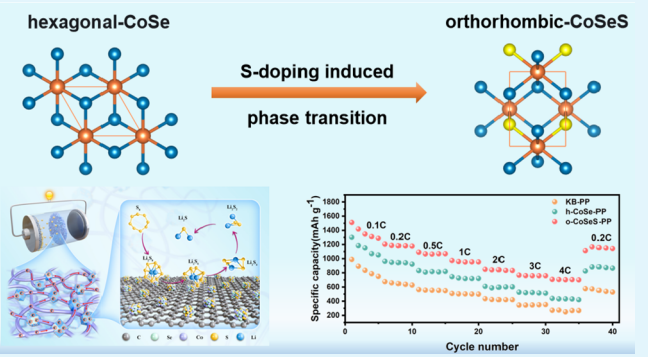


**KEYWORDS:** *root-nodule structure, phase transition, spin-mediated, lithium−sulfur batteries*



## 1. INTRODUCTION

Lithium−sulfur (Li−S) batteries have emerged as promising candidates for next-generation energy storage systems due to their high theoretical energy density of 2600 Wh $kg^{-1}$.[1−4] However, their practical application faces several challenges, including the insulating nature of sulfur and lithium sulfide, the dissolution of lithium polysulfides (LiPSs), and sluggish redox kinetics during cycling.[5−9] To address these issues, extensive efforts have been devoted to developing catalysts that can effectively adsorb and facilitate the conversion of LiPS intermediates.[6,10] In this context, biomimetic materials have offered innovative strategies for designing high-performance Li−S batteries by emulating the structural and functional features of natural systems.[11,12] Notable examples include bamboo-like nitrogen-doped carbon nanotubes developed by Zhang and co-workers[13] and a honeycomb-like three-dimensional nitrogen-doped porous carbon framework introduced by Yao and co-workers,[14] both of which demonstrated excellent LiPSs adsorption and conversion capabilities. Furthermore, bioinspired materials based on natural architectures such as ant nests,[15,16] sea urchins,[17] and red blood cells[18] feature unique hierarchical porous structures. These materials have shown distinct advantages, including a high specific surface area, making them attractive as host materials for sulfur cathodes.

Natural biological structures offer valuable paradigms for the design of advanced energy storage materials. The hierarchical interconnected architecture of root nodules, formed through symbiosis between plants and rhizobia, conceptually aligns well with the performance requirements of Li−S batteries. This structure can be conceptually mapped to the conductive framework of Li−S electrodes, establishing efficient pathways for ion and electron transport, thereby mitigating the sluggish redox kinetics caused by the insulating nature of sulfur and lithium sulfide. Meanwhile, the abundant hierarchical pores and interfaces in root nodules provide the electrode with a high

Received: September 28, 2025
Revised: December 31, 2025
Accepted: January 3, 2026
Published: January 10, 2026

specific surface area and a dense distribution of exposed catalytically active sites, which not only enhance polysulfide adsorption but also accelerate conversion kinetics, helping to suppress the shuttle effect. Furthermore, the inherent structural elasticity of root nodules, which accommodates volume changes during nitrogen fixation and nutrient exchange, is beneficial for buffering the volume change of sulfur during charge−discharge cycling, thereby improving the structural stability of the electrode. Thus, the root-nodule-inspired design can simultaneously address three key challenges in Li−S batteries: sluggish reaction kinetics, polysulfide shuttling, and substantial volume variation, laying a foundation for the development of high-performance Li−S batteries. Drawing inspiration from this structure offers a pathway for developing more efficient and stable catalytic materials.

In this study, inspired by the root-nodule system, we developed a biomimetic catalytic material that mimics its structural and functional characteristics. Using bacterial cellulose (BC) as a structural template and an ethylenediaminetetraacetic acid (EDTA)-mediated strategy, we constructed a carbon-supported cobalt selenide catalyst with a hexagonal phase (h-CoSe@C). Subsequent sulfurization treatment induced a phase transformation from hexagonal to orthorhombic structure, resulting in an orthorhombic cobalt selenide sulfide catalyst supported on carbon (o-CoSeS@C). When o-CoSeS@C was applied as a modifier of the separator in Li−S batteries, it delivered an initial discharge capacity of 1509 mAh $g^{-1}$ at 0.1 C and maintained a capacity decay rate as low as 0.057% per cycle over 1000 cycles at 1 C, demonstrating exceptional sulfur utilization and cycling stability. The excellent capacity retention exhibited by o-CoSeS@C implies that the introduced S-doping combined with carbon encapsulation may synergistically enhance structural stability plausibly through mechanisms analogous to those reported. Density functional theory (DFT) calculations further revealed that the high-spin electronic configuration of o-CoSeS@C enhances the overlap between Co d-orbitals and LiPSs p-orbitals, thereby strengthening adsorption and accelerating the catalytic conversion of LiPSs. This work provides valuable insights into the design of high-performance biomimetic catalysts through nonmetal doping and electronic structure regulation, offering a promising avenue for practical Li−S battery applications.

## 2. EXPERIMENTAL SECTION

### 2.1. Preparation of BC-EDTA Aerogel

Solvothermal techniques were frequently employed to develop BC and EDTAD composite aerogels. Following the ultrasonic dispersion of 4.5 mmol of EDTAD in N, N-dimethylformamide (DMF), 5 mL of pyridine was introduced as a stabilizer under continuous stirring. Subsequently, 300 mg of freeze-dried BC aerogel was mixed with the aforementioned solution, stirred for 2 h, and ultrasonicated to achieve a uniform dispersion. The resulting mixture was then transferred to a vacuum flask for air elimination and subjected to a hydrothermal reaction at 70 °C for 20 h. After the reaction, the resulting solution was centrifuged and stored for subsequent use.

### 2.2. Preparation of BC-E-Co Aerogel

Initially, 20 mmol of cobalt nitrate hexahydrate ($Co(NO_3)_2{\cdot}6H_2O$) was dissolved in 80 mL of DMF and subjected to ultrasonication to achieve a uniform dispersion. The fabricated BC-EDTA composite material was subsequently added to this solution, stirred for 6 h, and transferred to a vacuum flask to remove air. The mixture was then subjected to hydrothermal processing at 75 °C for 10 h. After centrifugation, a purple gel was obtained and stored for further use.

### 2.3. Preparation of BC-E-Co-ZIF Aerogel

To prepare the BC-E-Co-ZIF aerogel, 40 mmol of 2-methylimidazole (2-MIM) was dissolved in 100 g of methanol under constant stirring to ensure a complete and uniform dispersion. Subsequently, BC-E-Co aerogel was added to the mixture, which was stirred continuously for 6 h. Following this process, the composite material was rinsed multiple times with ethanol and deionized water to eliminate any residual ions. Finally, freeze-drying was performed to obtain the BC-E-Co-ZIF aerogel.

### 2.4. Preparation of BC-Co-ZIF Aerogel

Solution A was prepared by dispersing 300 mg of freeze-dried BC aerogel in 60 g of methanol under agitation. Methanol (20 g) was equally distributed into two beakers, designated solutions B and C. Solution B comprised 4 mmol of $Co(NO_3)_2{\cdot}6H_2O$, and solution C comprised 10 mmol of 2-MIM. Subsequently, solutions B and C were progressively incorporated into solution A under continuous agitation for 6 h. The resultant composite material was extensively washed with ethanol and deionized water to eliminate any residual ions. The BC-Co-ZIF aerogel was obtained by freeze-drying.

### 2.5. Preparation of h-CoSe@C Catalytic Material

To achieve a consistent distribution of the freeze-dried BC-E-Co-ZIF aerogel, it was placed in a quartz tube that was sealed at one end. Subsequently, 0.8 g of selenium powder was measured and positioned on either side of the BC-E-Co-ZIF aerogel. The quartz tube was placed in a tube furnace and subjected to heat treatment at 800 °C at a rate of 2 °C $min^{-1}$ under an argon atmosphere for 2 h. Subsequently, the system was cooled to ambient temperature, after which the sample was extracted and ground to yield the final hexagonal cobalt selenide carbon (h-CoSe@C) composite material.

### 2.6. Preparation of o-CoSeS@C Catalytic Material

S and h-CoSe @C were combined in a 5:1 mass ratio via chemical vapor deposition (CVD). The h-CoSe@C specimen was placed at the center of a quartz tube with S positioned at the inlet of the tube. Subsequently, the quartz tube was heated to 420 °C in a tube furnace under an argon atmosphere at a rate of 2 °C $min^{-1}$ for 2 h. Subsequently, the system was cooled to ambient temperature. The sample was then extracted and ground to obtain the o-CoSeS@C composite material.

### 2.7. h-CoSe@C- and o-CoSeS@C-Modified Separators

The as-synthesized o-CoSeS@C, Ketjen black (KB), and polyvinylidene fluoride (PVDF) were mixed in *N*-methyl-2-pyrrolidinone (NMP) at a mass ratio of 8:1:1 and stirred for 12 h to form a uniform slurry. This slurry was then applied to the clean, flat surface of polypropylene (PP) separators (Celgard 2400) to modify them. After drying, the separators were cut into 19 mm diameter circular disks. For comparison, h-CoSe@C-modified separators were prepared using the same method

### 2.8. Preparation of Sulfur Electrodes

To prepare the sulfur electrodes, a melt-diffusion method was employed. First, 75 wt % sublimed sulfur and 25 wt %KB were blended and finely ground to form a homogeneous mixture. This mixture was then sealed in an argon atmosphere and heated at 155 °C for 12 h. The resulting sulfur composite was combined with additional KB and PVDF in a mass ratio of 7:2:1, dissolved in NMP to produce a smooth slurry. This slurry was applied onto an aluminum foil current collector and dried under vacuum at 60 °C for 12 h. Afterward, the electrodes were punched into 12 mm diameter disks, with an areal sulfur loading of approximately 0.8 mg·$cm^{-2}$.

### 2.9. Material Characterization

Scanning electron microscopy (SEM, Zeiss Sigma 300) was used to examine the morphologies of the prepared samples. To examine the structures of the samples, various analytical techniques were employed, including Fourier-transform infrared (FTIR) spectroscopy,


https://doi.org/10.1021/acsami.5c19431
ACS Appl. Mater. Interfaces 2026, 18, 4779−4791

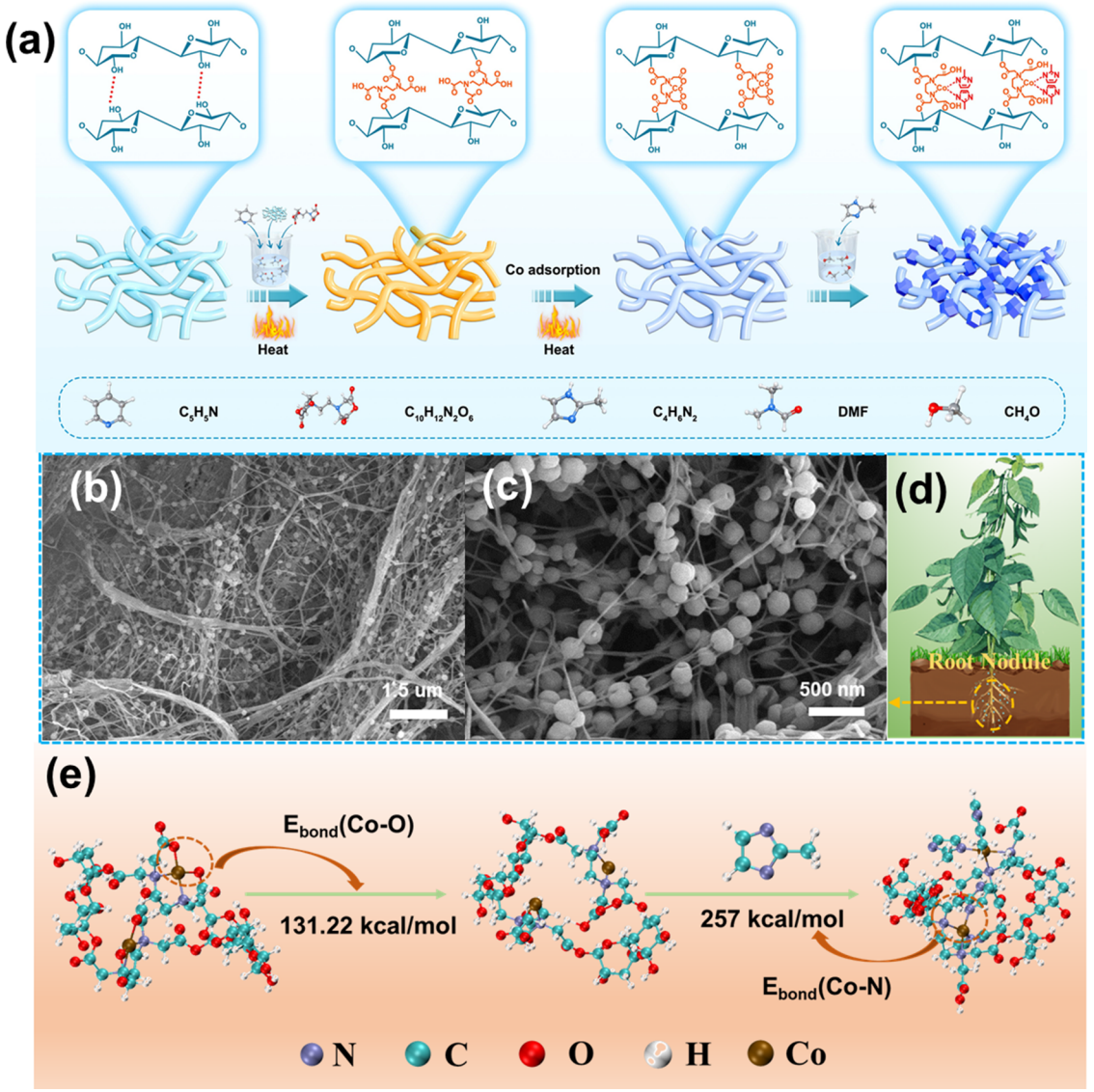


**Figure 1.** (a) Schematic representation of the synthesis method for BC-E-Co-ZIF; (b, c) SEM image of BC-E-Co-ZIF; (d) structure of the root nodules of plants; (e) simulation of bond energy for Co−O and Co−N in BC-E-Co and BC-E-Co-ZIF structures.

X-ray diffraction (Bruker, Advanced D8A A25), Raman spectroscopy (Thermo Scientific DXR3), and X-ray photoelectron spectroscopy (XPS, Thermo ESCALAB 250XI).

### 2.10. Electrochemical Characterization

Electrochemical investigations of Li−S batteries were conducted using CR2032 coin cells, employing KB/S as the cathode, lithium metal as the anode, and a modified separator. A 1 M solution of lithium bis(trifluoromethanesulfonyl) imide (LiTFSI) in a 1:1 volume mixture of dioxolane (DOL) and dimethoxyethane (DME) containing 1 wt % $LiNO_3$ was used as the electrolyte. The ratio of electrolyte to sulfur (E/S) in the half-cell was 5 $\mu$L $mg^{-1}$. Galvanostatic charge−discharge cycle behaviors were conducted on an automated battery test station (LAND CT2001A) within a potential range of 1.7−2.8 V at various C-rates (1.0 C = 1675 mA $g^{-1}$). Electrochemical impedance spectroscopy (EIS) in the 0.01−100 kHz frequency range and cyclic voltammetry (CV) were performed using an Autolab 302 N electrochemical workstation.

### 2.11. Experiments on $Li_2S$ Nucleation

A $Li_2S_8$(0.2 mmol. $L^{-1}$) solution was prepared by reacting sulfur and $Li_2S$ in a 7:1 stoichiometric ratio in tetraglyme, followed by continuous magnetic stirring at 60 °C for 24 h. The cathode was fabricated by mixing the active materials with PVDF in a 9:1 mass ratio in NMP. The subsequent fabrication steps were the same as those used for the lithium−sulfur battery (LSB) electrodes. A total of 15 $\mu$L of $Li_2S_8$ electrolyte and 15 $\mu$L of blank electrolyte (without $Li_2S_8$) were separately dropped onto both sides of the separator. The batteries were initially discharged at 0.112 mA to 2.10 V, followed by a potentiostatic hold at 2.09 V for $Li_2S$ deposition.

### 2.12. Experiments on Symmetric Cells

A $Li_2S_6$-based LiTFSI electrolyte with a concentration of 0.5 m was configured by adding sublimated sulfur in a molar ratio of 5:1 to $Li_2S$. The active materials (h-CoSe@C and o-CoSeS@C), KB, and PVDF were ground in NMP at a ratio of 8:1:1 and uniformly coated on Al foil. After being dried, two identical positive and negative electrodes were assembled with polypropylene (PP) separators to form symmetric cells. The CV voltage range was from −1.0 to 1.0 V at 50 mV $s^{-1}$.

## 3. RESULTS AND DISCUSSION

As shown in Figure 1a, this work successfully utilized BC as a template and employed an EDTA-assisted site-specific growth strategy to prepare a cobalt-based zeolitic imidazolate framework aerogel (BC-E-Co-ZIF) with a root-nodule structure.



https://doi.org/10.1021/acsami.5c19431
ACS Appl. Mater. Interfaces 2026, 18, 4779−4791

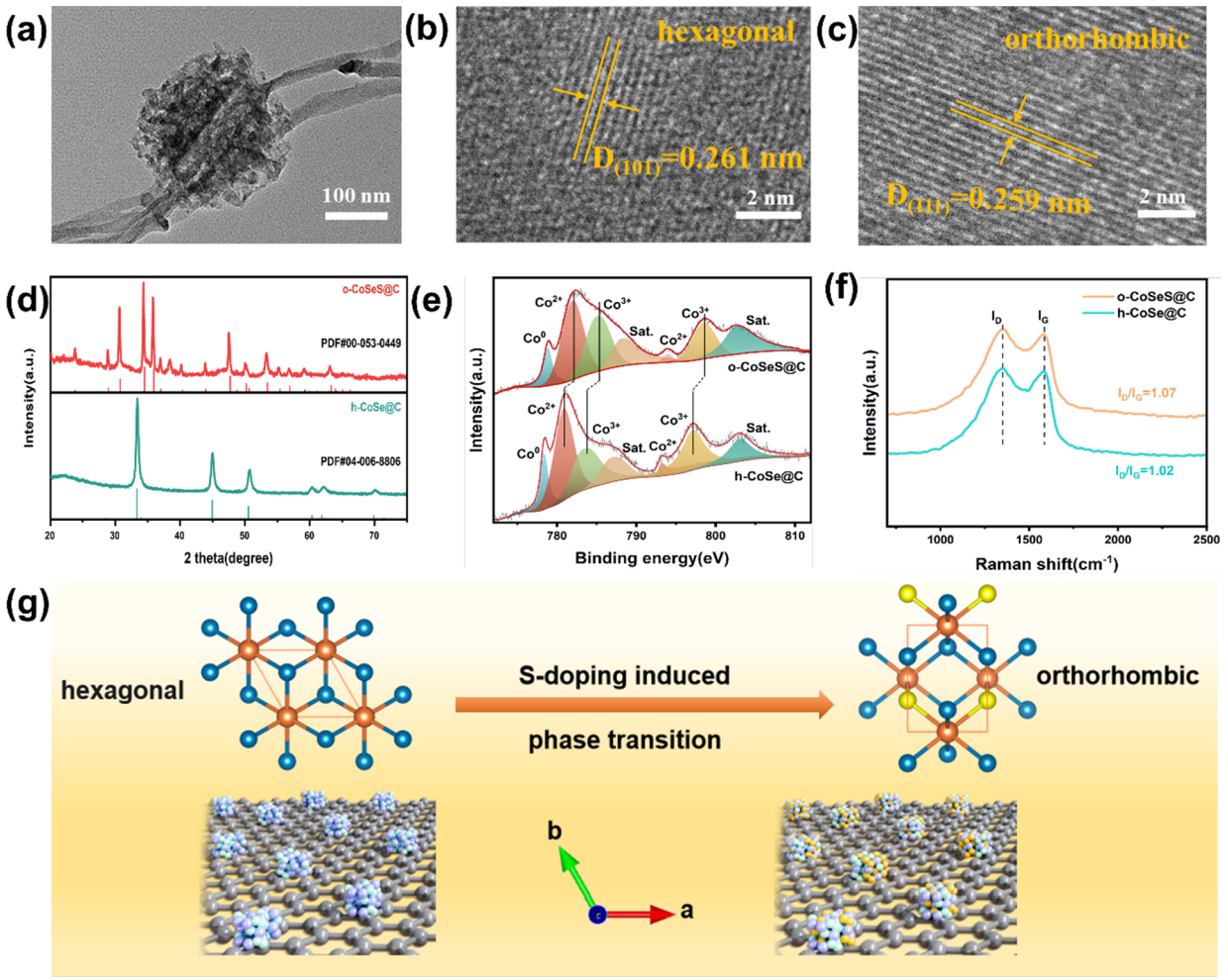


**Figure 2.** (a) TEM image of o-CoSeS@C; (b) HR-TEM image of h-CoSe@C; (c) HR-TEM image of o-CoSeS@C; (d) XRD patterns of h-CoSe@C and o-CoSeS@C; (e) high-resolution XPS spectra of Co 2p; (f) Raman spectra of h-CoSe@C and o-CoSeS@C; and (g) schamatic illustration of the phase transition process driven by sulfur doping.

Specifically, EDTA was first grafted onto the hydroxyl groups of BC through chemical bonding via a solvothermal method, resulting in EDTA-modified BC (denoted as BC-E). Subsequently, BC-E was immersed in a $Co(NO_3)_2{\cdot}6H_2O$ solution to adsorb $Co^{2+}$ ions (BC-E-Co). After adsorption saturation was reached, the sample was transferred to a methanol solution containing 2-methylimidazole (2-MIM) to facilitate the growth of Co-ZIF on the BC template. The interaction between BC and EDTA was analyzed with Fourier-transform infrared spectroscopy (FTIR). Compared to pure BC, the BC-E aerogel exhibited a new characteristic absorption peak at 1740 $cm^{-1}$[19] (Figure S1a,b Supporting Information), which was attributed to the chemical bonding between the carboxyl groups of EDTA and the hydroxyl groups of BC. EDTA can serve as an adsorption site for metal ions, not only promoting the uniform distribution of $Co^{2+}$ but also accelerating the nucleation and growth process of Co-ZIF. The structure of the BC-E-Co-ZIF aerogel was characterized using X-ray diffraction (XRD) (Figure S2, Supporting Information), and the results showed that its diffraction peaks were highly consistent with the standard structure of Co-ZIF,[20] indicating its successful formation. The SEM images of BC-E-Co-ZIF (Figure 1b,c) demonstrated that Co-ZIF particles were uniformly anchored on the BC nanofibers, exhibiting a distinctive root-nodule-like morphology (Figure 1d). DFT calculation was employed to investigate the growth mechanism of BC-E-Co-ZIF. As shown in Figure 1e, in the BC-E-Co framework, the Co atom formed coordination bonds with two nitrogen and two oxygen atoms, where the Co−O and Co−N bond energies were 131.22 and 257 kcal $mol^{-1}$. This result indicated that the Co−N coordination exhibited a stronger affinity. Consequently, when 2-MIM was added to the methanol solution containing BC-E-Co, the initial equilibrium of the system was disrupted due to the higher bond energy and stronger binding force of the Co−N bond, leading to the breaking of Co−O bonds and the formation of new Co−N bonds. The above result was further confirmed by the independent gradient model analysis (Figure S3a,b, Supporting Information). The BC-E-Co-ZIF precursor was initially selenized at 800 °C, yielding a carbon-based CoSe catalyst with a hexagonal phase structure, which was denoted as h-CoSe@C. Subsequently, sulfur doping was performed, resulting in the formation of carbon-based CoSeS with an orthorhombic phase structure (designated as o-CoSeS@C). SEM analysis (Figure S4, Supporting Information) demonstrated that the Co-ZIF framework retained its root-nodule structure during the reactions, confirming its exceptional structural stability. Additionally, the TEM characterization of o-CoSeS@C (Figure 2a) revealed the formation of a highly ordered porous structure. High-resolution TEM analysis


https://doi.org/10.1021/acsami.5c19431
ACS Appl. Mater. Interfaces 2026, 18, 4779−4791

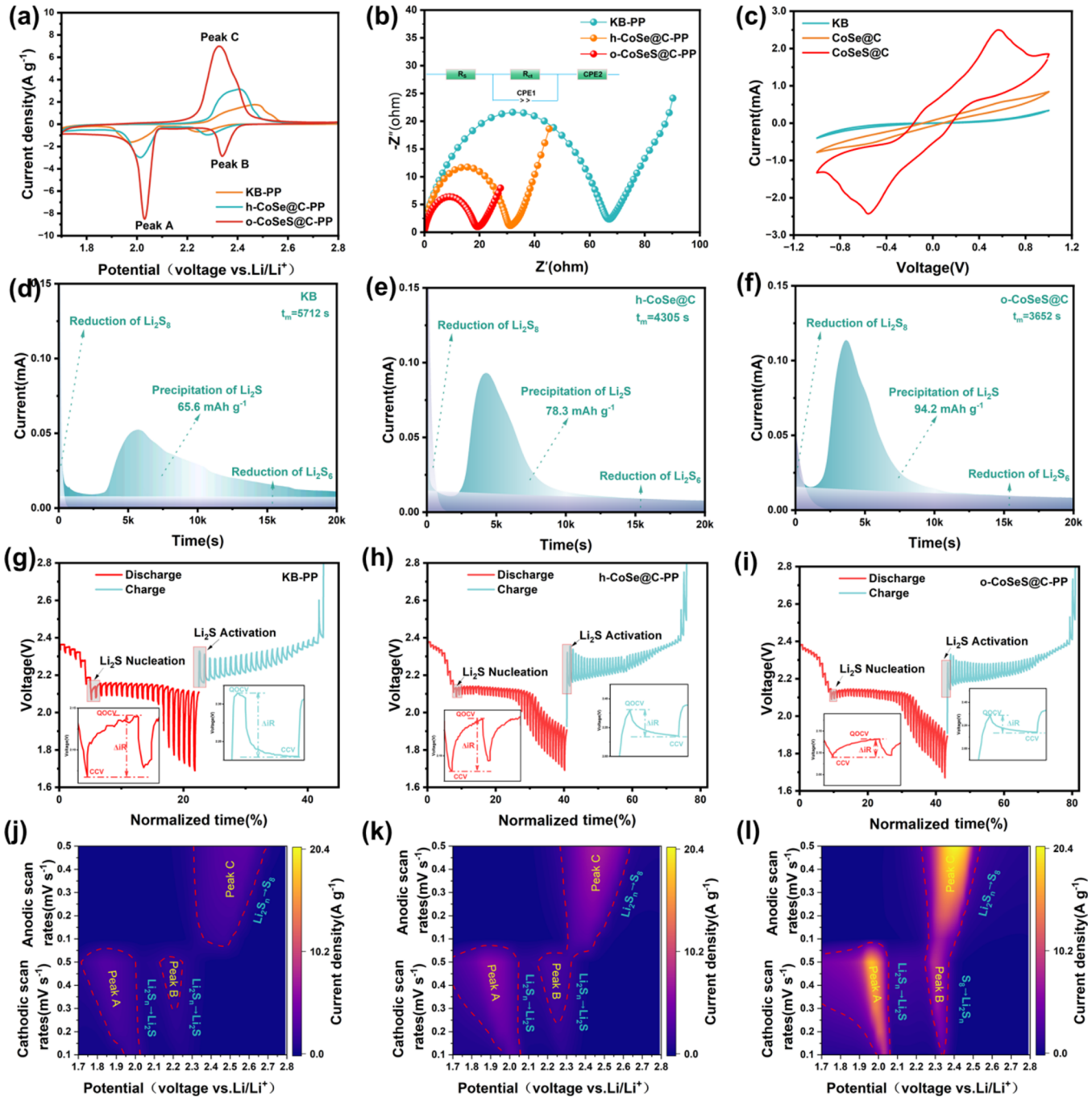


**Figure 3.** Electrochemical characterization of h-CoSe@C and o-CoSeS@C membrane-modified batteries. (a) CV curves; (b) EIS impedance spectra; (c) CV curve of symmetric batteries; (d–f) $Li_2S$ deposition profiles; (g–i) GITT curves; and (j–l) contour maps of CV curves at different scan rates.

(Figure 2b) exhibited lattice fringes with an interplanar spacing of 0.261 nm, corresponding to the (1 0 1) plane of hexagonal $CoSe_2$,[21] while Figure 2c displayed lattice fringes with a spacing of 0.259 nm, characteristic of the (111) plane of orthorhombic $CoSe_2$.[22] The XRD pattern (Figure 2d) confirmed a hexagonal crystal structure of h-CoSe@C after high-temperature selenization with the main characteristic peaks at 33.3, 44.7, 50.6, 60.4, 61.9, 69.9, and 71.3°, corresponding to the (101), (102), (110), (103), (112), (202), and (004) crystal planes, respectively.[23] While the XRD pattern of o-CoSeS@C exhibited principal peaks at 30.7, 34.5, 35.9, and 47.7°, which correspond to the (011), (101), (111), and (120) crystal planes, respectively. Thus, sulfur doping induced a substantial phase transition, converting the structure into an orthorhombic structure in o-CoSeS@C. To exclude the influence of temperature and time on the phase transition and confirm the crucial role of sulfur doping, a strict control experiment under identical conditions was designed. As shown in Figure S5, the h-CoSe@C sample (without sulfur doping) was subjected to the same heat treatment process as the sulfur-doped o-CoSeS@C sample, including an identical heating temperature, holding time, and cooling rate (consistent with the experimental parameters described in the Section 2). Subsequent XRD characterization of the heat-treated h-CoSe@


https://doi.org/10.1021/acsami.5c19431
ACS Appl. Mater. Interfaces 2026, 18, 4779–4791

C sample showed no discernible shifts in diffraction peaks or emergence of new phases (consistent with the original h-CoSe phase, JCPDS #04-006-8806), confirming that the heat treatment conditions alone do not induce phase transition. X-ray photoelectron spectroscopy (XPS) was further employed to analyze the elemental valence states and electronic structures of o-CoSeS@C and h-CoSe@C. As shown in Figure 2e, the Co 2p spectra of h-CoSe@C exhibited two main $Co^{2+}$ peaks at 780.84 eV (Co $2p_{3/2}$) and 793.19 eV (Co $2p_{1/2}$), respectively, while the satellite peaks at 783.29 and 797.12 eV were attributed to the presence of $Co^{3+}$. The above results indicated that cobalt predominantly existed as $Co^{2+}$ and $Co^{3+}$ in h-CoSe@C. Notably, after sulfur doping, the binding energies of Co $2p_{3/2}$ and Co $2p_{1/2}$ in o-CoSeS@C shifted to higher energies by approximately 1.12 and 0.76 eV, respectively. This upward shift suggests that sulfur doping induced electron withdrawal from Co sites, leading to a higher oxidation state (or enhanced electron localization) at the metal centers. Se 3d spectra of both h-CoSe@C and o-CoSeS@C (Figure S6a, Supporting Information) exhibit four principal peaks, while the S 2p spectra analysis revealed multiple chemical states of sulfur (Figure S6b, Supporting Information). The disorder of carbon in the prepared materials was studied with Raman spectroscopies (Figure 2f) of h-CoSe@C and o-CoSeS@C. The degree of defects in carbon materials was usually quantitatively evaluated using the intensity ratio of $I_D/I_G$.[24,25] The ratio for h-CoSe@C was 1.02, slightly lower than that of o-CoSeS@C (1.07). This suggested that sulfur doping reduced the graphitization degree of the carbon material.[26] The above structural transformation from h-CoSe@C to o-CoSeS@C is illustrated in Figure 2g.

Membrane modification technology was proven to significantly suppress the polysulfide shuttle effect in Li−S batteries.[27,28] Based on it, this study modified the separator with CoSe catalysts. The surface of an untreated polypropylene (PP) separator contained multiple submicron-sized pores, which provided pathways for LiPS shuttling, leading to significant degradation in battery performance (Figure S7a, Supporting Information). In contrast, the o-CoSeS@C-modified separator exhibited a denser surface with enhanced LiPS adsorption capability (Figure S7b, Supporting Information), effectively suppressing the shuttle effect. The SEM analysis of the separator's cross-section (Figure S7c, Supporting Information) demonstrated a well-formed interface between the modification layer and the PP separator. The thickness of the modified layer was observed to be only 6.5 $\mu$m, indicating minimal impact on the energy density of the battery. Additionally, the elemental distribution mapping of the cross-section (Figure S7d, Supporting Information) showed a uniform distribution of C, O, Co, Se, and S elements within the material. Meanwhile, the wettability and electrolyte affinity of the interface of h-CoSe@C-, and o-CoSeS@C-modified membranes were greatly enhanced (Figure S8, Supporting Information). These modifications promoted uniform LiPS diffusion and accelerated their conversion, effectively suppressing the shuttle effect.[29] Figure 3a presents the cyclic voltammetry (CV) curves of batteries with PP separators and h-CoSe@C and o-CoSeS@C-modified separators (denoted as PP, h-CoSe@C, and o-CoSeS@C battery). The results revealed that the CV curves of all three batteries exhibited typical Li−S battery redox characteristics, including one oxidation peak and two reduction peaks.[30] Notably, the o-CoSeS@C battery exhibited significantly enhanced current density responses in the CV curves, confirming the superior electrocatalytic performance of o-CoSeS@C. The potential positions of the corresponding redox peaks (Figure S9, Supporting Information) directly reflected the polarization degree of the electrode reaction,[31] where the potential difference ($\Delta E$) between the oxidation peak ($C$) and the reduction peak ($A$). The polarization potential of the o-CoSeS@C battery was only 0.29 V, representing a 27.5% reduction compared to that of the h-CoSe@C battery (0.4 V) and a 42% reduction compared to that of the unmodified PP separator battery (0.5 V). This further confirmed the exceptional catalytic performance of o-CoSeS@C in promoting LiPS conversion reactions.[31] Figure 3b displays the Nyquist plots of the PP, h-CoSe@C, and o-CoSeS@C battery. It revealed that the impedance arc radius of the o-CoSeS@C battery was significantly smaller than that of the other two batteries, indicating a notable reduction of charge transfer resistance ($R_{ct}$). For further quantitative analysis, the $R_{ct}$ of the o-CoSeS@C battery was only 17.9 Ω, representing a 40.1% reduction compared to the h-CoSe@C battery (29.9 Ω) and a 73.2% reduction compared to the unmodified PP battery (66.8 Ω) (Figure S10, Supporting Information). This significant reduction in impedance demonstrated the excellent electrochemical activity of the o-CoSeS@C modification layer at the electrode interface, effectively promoting electron transfer during LiPS conversion reactions.[32] To investigate the catalytic performances of KB, h-CoSe@C, and o-CoSeS@C in the polysulfide redox process, symmetric cells with a $Li_2S_6$ electrolyte were assembled using these catalysts as electrode materials. As shown in Figure 3c, the o-CoSeS@C battery outperformed the KB and h-CoSe@C batteries, exhibiting a higher current density, a broader peak area, and a smaller polarization potential difference. These results demonstrated that the o-CoSe@C electrode possessed markedly superior catalytic performance in LiPSs redox reactions.[33] Constant potential discharge experiments were performed to investigate the influence of the three catalysts on the nucleation process. The KB electrode reached its peak current at 5712 s with a nucleation capacity of 65.6 mAh $g^{-1}$, as shown in Figure 3d. The h-CoSe@C electrode achieved its peak current at 4305 s, with an increased nucleation capacity of 78.3 mAh $g^{-1}$, while the o-CoSeS@C electrode exhibited its peak current at 3652 s, achieving the highest nucleation capacity of 94.2 mAh $g^{-1}$, as shown in Figure 3e,f. It also revealed that the nucleation time of the o-CoSeS@C electrode was reduced by 36.1 and 15.2% compared to those of KB and h-CoSe@C, respectively, and its nucleation capacity increased by 43.6 and 20.3%, respectively. The above results demonstrated that o-CoSeS@C could significantly reduce the energy barrier for $Li_2S$ nucleation and promote rapid LiPS deposition.[34] Furthermore, the galvanostatic intermittent titration technique (GITT) was employed to analyze changes in the interface resistance. All three batteries exhibited varying degrees of polarization during charge−discharge processes (Figures 3g−i and S11, Supporting Information). Specifically, the PP battery exhibited the highest polarization potentials with 72 mV during charging and 180 mV during discharging, indicating weak LiPS redox conversion capability and significant interfacial reaction resistance. In contrast, the h-CoSe@C battery showed significantly reduced polarization potentials, with 56 mV during charging and 170 mV during discharging, representing reductions of 22.2 and 5.6%, respectively, compared to the PP battery. The o-CoSeS@C battery exhibited the smallest


https://doi.org/10.1021/acsami.5c19431
ACS Appl. Mater. Interfaces 2026, 18, 4779−4791

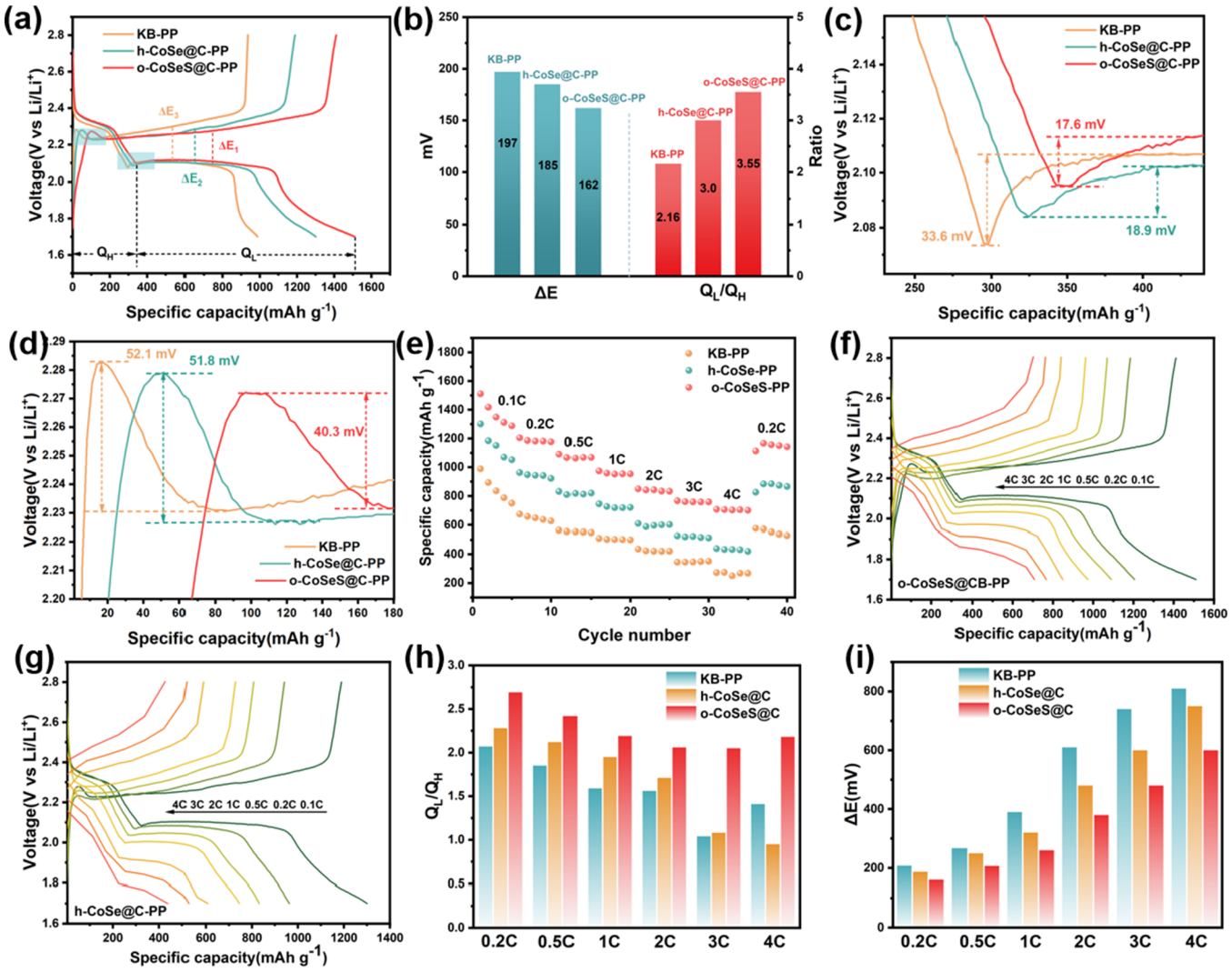


**Figure 4.** (a) First cycle charge−discharge curves of batteries with PP, h-CoSe@C, and o-CoSeS@C modified membranes at 0.1C; (b) $\Delta E$ values and $Q_L/Q_H$ ratios; (c) local magnification of the discharge curve; (d) local magnification of the charge curve; (e) rate performance; (f, g) first cycle charge−discharge curves at different rates; (h) $Q_L/Q_H$; and (i) overpotential.

polarization, with 40 mV during charging and 145 mV during discharging, corresponding to reductions of 44.4 and 19.4%, respectively, compared to the PP battery. These results demonstrated that separator modification strategies significantly affected the kinetics and interfacial reaction resistance of Li−S batteries. In particular, the introduction of o-CoSeS@C not only effectively reduced polarization potentials and interfacial reaction resistance during charge−discharge processes but also significantly enhanced LiPSs redox kinetics.[35,36] The CV curves of PP, h-CoSe@C, and o-CoSeS@C batteries at scan rates of 0.1, 0.2, 0.3, 0.4, and 0.5 mV/s (Figure S12a−c, Supporting Information) show that the redox peak currents of the o-CoSeS@C battery were significantly higher than those of the h-CoSe@C battery and the PP battery, demonstrating that o-CoSeS@C exhibited superior catalytic performance and stronger kinetic regulation capabilities.[3] As shown in Figure 3j−l, the contour map of the o-CoSeS@C battery displayed a distinct oxidation peak corresponding to the oxidation of $Li_2S_2/Li_2S$ to $S_8$, as well as two reduction peaks corresponding to the reduction of $S_8$ to $Li_2S_x$ ($x$ = 4, 6, and 8) and the further reduction of higher-order LiPSs to $Li_2S_2/Li_2S$. In contrast, the contour maps of the PP battery and the h-CoSe@C battery exhibited blurred peaks and peak shifts, indicating lower LiPS conversion efficiency and slower reaction kinetics. These results confirmed that the o-CoSeS@C separator modification significantly enhanced LiPS catalytic conversion and reaction kinetics in Li−S batteries.[37] The relationship between CV peak currents and the scan rate was analyzed to evaluate the impact of separator modifications on LiPS redox kinetics. The peak currents of all three separator-modified batteries exhibited a good linear relationship with the square root of the scan rate (Figure S13a−c, Supporting Information), suggesting that the electrochemical reaction rate in the system was primarily limited by the diffusion rate of reactants (such as LiPSs or lithium ions). The slopes for the o-CoSeS@C battery were 550, 370, and 1070, significantly higher than 110, 70, and 330 for the h-CoSe@C battery and 70, 40, and 130 for the PP battery (Figure S13d, Supporting Information). It confirmed that the former one had the fastest diffusion kinetics, greatest catalytic activity, and highest reaction rates.[38,39] The diffusion coefficients of lithium ions were computed using the Randles−Sevcik equation.[40,41] The calculated $Li^+$ diffusion coefficients, summarized in Table S1 (Supporting Information), further support these findings. These results demonstrated that the o-


https://doi.org/10.1021/acsami.5c19431
ACS Appl. Mater. Interfaces 2026, 18, 4779−4791

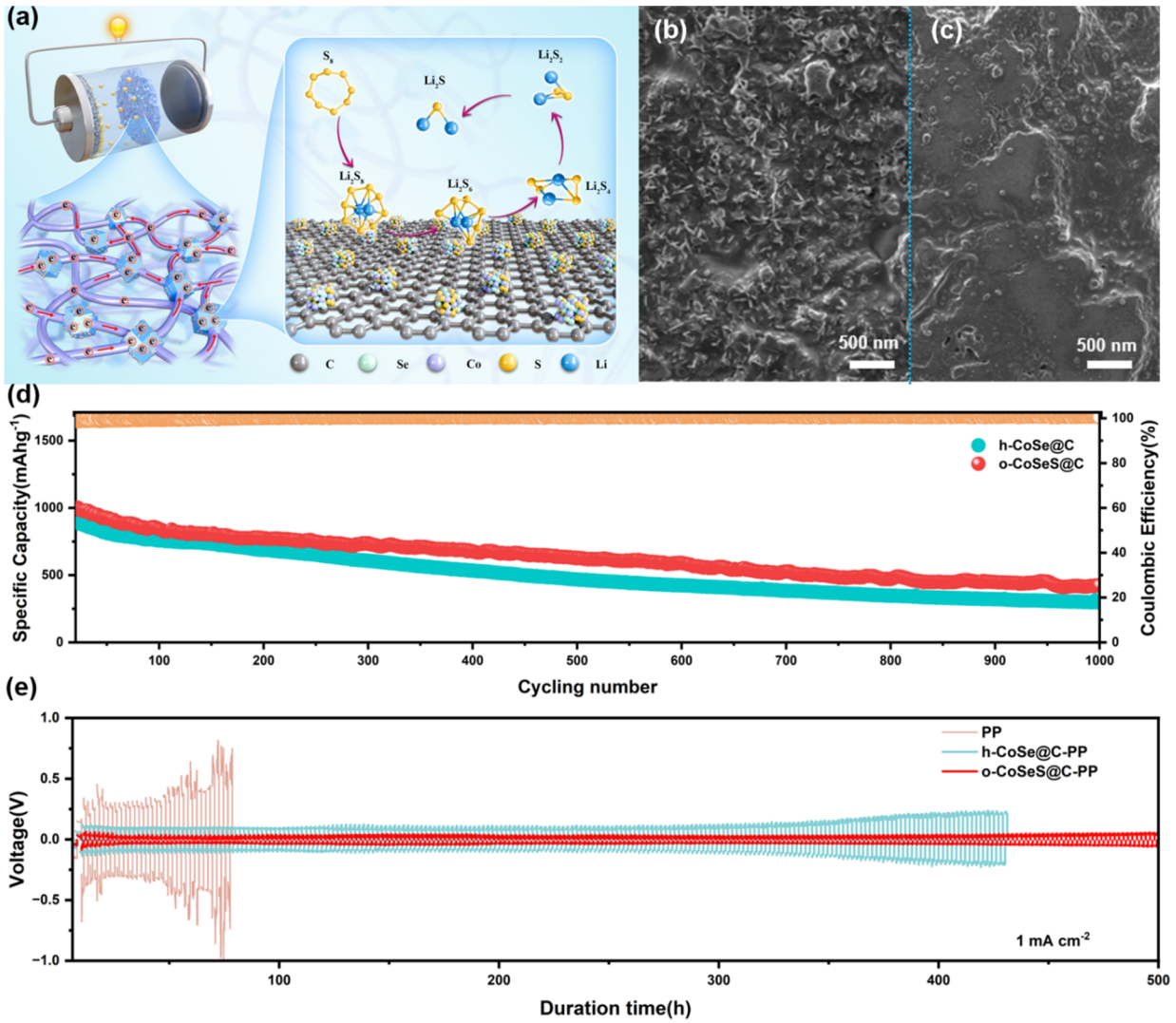


**Figure 5.** (a) Schematic representation of the working principle of the o-CoSeS@C modified membrane Li−S battery; SEM images of the Li anode surface after 200 cycles at 1C for (b) h-CoSe@C; (c) o-CoSeS@C modified membrane batteries; (d) cycle stability test of batteries with h-CoSe@C and o-CoSeS@C modified membranes at 1C, and (e) cycle stability of Li/Li symmetric batteries with PP, h-CoSe@C, and o-CoSeS@C modified membranes at 1 mA $cm^{-2}$.

CoSeS@C modification strategy could significantly reduce diffusion resistance, promote reaction kinetics, and enhance LiPS conversion efficiency.

Constant current charge−discharge tests at 0.1 C revealed charge−discharge curves with a charge plateau and two discharge plateaus, aligning with the oxidation and reduction peaks observed in the CV curves (Figure 4a).[42] The initial cycle discharge capacity of the o-CoSeS@C battery was 1509 mAh $g^{-1}$, significantly higher than that (1301 mAh $g^{-1}$) of the h-CoSe@C battery and that (988 mAh $g^{-1}$) of the PP battery. The capacity ratio between the lower ($Q_L$) and upper ($Q_H$) discharge plateaus is essential for evaluating the catalytic performance in the conversion of soluble LiPSs. Subsequently, the overpotentials and $Q_L/Q_H$ ratios of the three batteries during the charge−discharge cycles were examined. As shown in Figure 4b, the overpotential of the o-CoSeS@C battery was 162 mV, significantly lower than that (185 mV) of the h-CoSe@C battery and that (197 mV) of the PP battery. Notably, the $Q_L/Q_H$ ratio of the o-CoSeS@C battery reached 3.55, significantly higher than those of the h-CoSe@C battery (3.0) and the PP battery (2.16). This enhanced ratio demonstrated the superior catalytic capability of the o-CoSeS@C battery in facilitating the conversion of long-chain LiPSs to short-chain LiPSs, thereby effectively mitigating the shuttle effect.[43] Furthermore, as shown in Figure 4c,d, the polarization potentials of the o-CoSeS@C battery were 17.6 and 40.3 mV, significantly lower than those (18.9 and 51.8 mV) of the h-CoSe@C battery and those (33.6 and 52.1 mV) of the PP battery. This demonstrated that o-CoSeS@C could effectively reduce polarization during charge−discharge processes, thereby improving electrochemical reaction kinetics. Rate performance tests were conducted on the PP, h-CoSe@C, and o-CoSeS@C batteries. As shown in Figure 4e, the o-CoSeS@C battery delivered outstanding discharge capacities of 1509, 1205, 1090, 973, 849, and 767 mAh $g^{-1}$, at current densities of 0.1, 0.2, 0.5, 1, 2, and 3 C, respectively. Notably, even at a high current density of 4 C, its discharge capacity remained at a high level of 707 mAh $g^{-1}$, significantly outperforming those of the h-CoSe@C battery and the PP battery. Furthermore, when the current density was reduced back to 0.2 C, the capacity of the o-CoSeS@C battery recovered to 1166 mAh $g^{-1}$, demonstrating excellent capacity


https://doi.org/10.1021/acsami.5c19431
ACS Appl. Mater. Interfaces 2026, 18, 4779−4791

retention and cycling stability. In contrast, the capacities of the h-CoSe@C battery at the same rates were 1301, 962, 831, 745, 608, 526, and 438 mAh $g^{-1}$, while the capacities of the PP battery were only 988, 674, 563, 508, 435, 344, and 272 mAh $g^{-1}$, showing significant capacity decay and poor rate performance. The o-CoSeS@C battery exhibited clear charge−discharge plateaus even at a high current density of 4 C (Figures 4f−g and S14, Supporting Information), indicating that it could maintain efficient LiPSs conversion reaction kinetics under high-rate conditions. Additionally, Figure 4h−i shows the first-cycle charge−discharge overpotentials and $Q_L/Q_H$ ratios of the three batteries at different rates. The results demonstrated that the o-CoSeS@C battery exhibited smaller overpotentials and higher $Q_L/Q_H$ ratios at all current densities. Specifically, the overpotential of the o-CoSeS@C battery at 4 C was only 215 mV, significantly lower than that of the h-CoSe@C battery (278 mV) and the PP battery (312 mV). Meanwhile, its $Q_L/Q_H$ ratio at 4 C remained at 1.08, higher than that of the h-CoSe@C battery (1.03) and the PP battery (1.01). These results further confirmed that the o-CoSeS@C separator modification material could effectively reduce the activation energy of LiPS conversion reactions and significantly enhance the reaction kinetics.

Figure 5a depicts the working mechanism of the o-CoSeS@C battery. This catalytic material draws inspiration from the symbiotic structure between rhizobia and plant roots, simulating their efficient material transport and energy exchange mechanisms. During the formation of the root-nodule structure, EDTA acted as a crucial additive, facilitating a robust interaction between Co-ZIF and BC. This structure enabled electrons to rapidly reach the active sites of CoSe, significantly improving the adsorption and conversion efficiency of LiPSs. Conversely, in the absence of EDTA, the connection between Co-ZIF and BC was noticeably weakened (Figure S15, Supporting Information). The rate performance of the battery using a CoSeS@C battery (without EDTA) Figure S16a, Supporting Information) reveals a substantial decline in the battery's capacity at different current densities, reflecting poor rate performance. Moreover, the initial discharge capacity was only 1283 mAh $g^{-1}$ at 0.1 C (Figure S16b, Supporting Information), significantly lower than that of the o-CoSeS@C-modified separator. These results highlighted that the exceptional performance of Li−S batteries could be significantly enhanced by the superior design of the biomimetic structure. To evaluate the effectiveness of h-CoSe@C and o-CoSeS@C batteries in suppressing the LiPS shuttle effect, batteries equipped with these membranes were cycled at a current density of 1 C for 200 cycles. Subsequently, the surfaces of the lithium anodes were examined using SEM. As shown in Figure 5b, after 200 cycles, the lithium anode surface of the h-CoSe@C battery exhibited numerous granular deposits. This phenomenon was primarily attributed to the migration of the dissolved LiPSs through the separator to the lithium metal anode surface, where they were converted to insoluble products. In contrast, the lithium metal anode surface of the o-CoSeS@C battery remained relatively smooth (Figure 5c). This study confirmed that the o-CoSeS@C battery provided a substantial advantage in controlling the LiPS shuttle effect. It also underscores its importance in facilitating the uniform deposition of lithium ions. Extended cycling performance tests were conducted to systematically evaluate the long-term stability of the batteries. As shown in Figure 5d, the o-CoSeS@C battery exhibited exceptional stability, with a capacity decay rate of only 0.057% per cycle over 1000 cycles at 1 C. In contrast, the h-CoSe@C battery experienced notable capacity degradation, with a decay rate of 0.066% over the same number of cycles. It is worth noting that catalytic materials operating in such environments often face potential challenges, including the migration and/or volatilization of Se and/or S species and lattice distortion induced by repeated cycling. Recent studies suggest that such degradation can be mitigated by strategies such as (i) heteroatom anchoring (e.g., P doping in $CoSe_2$ to stabilize Se vacancies) and (ii) carbon-matrix buffering and protection.[44−47] To validate the effectiveness of the o-CoSeS@C catalyst in practical high-energy density Li−S batteries, we systematically evaluated its electrochemical performance under lean electrolyte (low E/S ratio) and high sulfur loading conditions, key parameters for practical application. As shown in Figure S17, the o-CoSeS@C-based battery was tested at a current density of 0.2 C with a high sulfur loading of 3.9 mg $cm^{-2}$ and a lean electrolyte condition (E/S ratio = 5 $\mu$L $mg^{-1}$). Notably, the battery delivered an initial discharge specific capacity of 805 mAh $g^{-1}$ and maintained a reversible capacity of 765 mAh $g^{-1}$ after 100 cycles, corresponding to an average per-cycle capacity decay rate of only 0.05%. This outstanding stability under low E/S ratio conditions originates from the intrinsic advantages of the o-CoSeS@C catalyst: the sulfur-induced phase transition and high-spin Co electronic structure synergistically enhance LiPS adsorption (suppressing the shuttle effect even in a limited electrolyte) and accelerate catalytic conversion (improving sulfur utilization under high sulfur loading). Li/Li symmetric batteries were constructed by using PP-, h-CoSe@C-, and o-CoSeS@C-modified separators. As shown in Figure 5e, the battery employing the PP separator exhibited high localized overpotential, resulting in nonuniform lithium metal deposition and significant battery polarization within a short period (approximately 100 h). This result indicated that the unmodified PP separator was unable to effectively regulate the transport and deposition behavior of lithium ions, thereby limiting the battery's cycling stability. In contrast, the battery with the h-CoSe@C-modified separator exhibited enhanced ionic conductivity and improved interfacial stability, demonstrating significant polarization after 350 h. These results highlighted the importance of separator modification strategies in promoting uniform lithium deposition and enhancing the cycling performance. Notably, the battery with the o-CoSeS@C-modified separator demonstrated the most superior regulation effect. Over the extended 500 h test, its voltage curve remained highly stable, with negligible polarization observed. This excellent performance was primarily attributed to the high catalytic activity and abundant active sites of o-CoSeS@C, which effectively regulated the interfacial electron distribution and lithium-ion concentration gradient, thereby avoiding nonuniform deposition caused by localized electric field enhancement. DFT was employed to investigate the electronic structures, surface adsorption energies, and reaction pathways of the h-CoSe@C and o-CoSeS@C catalytic materials. The initial design of the adsorption model (Figure S18, Supporting Information) illustrates that the CoSe region contained most of the key reaction-active sites for both catalytic materials. To better represent their true catalytic capabilities, models were created using various phases of the CoSe catalysts. The total density of states (TDOS) before and after sulfur doping was used to investigate the effect of phase transitions induced by sulfur doping on the material's


https://doi.org/10.1021/acsami.5c19431
ACS Appl. Mater. Interfaces 2026, 18, 4779−4791

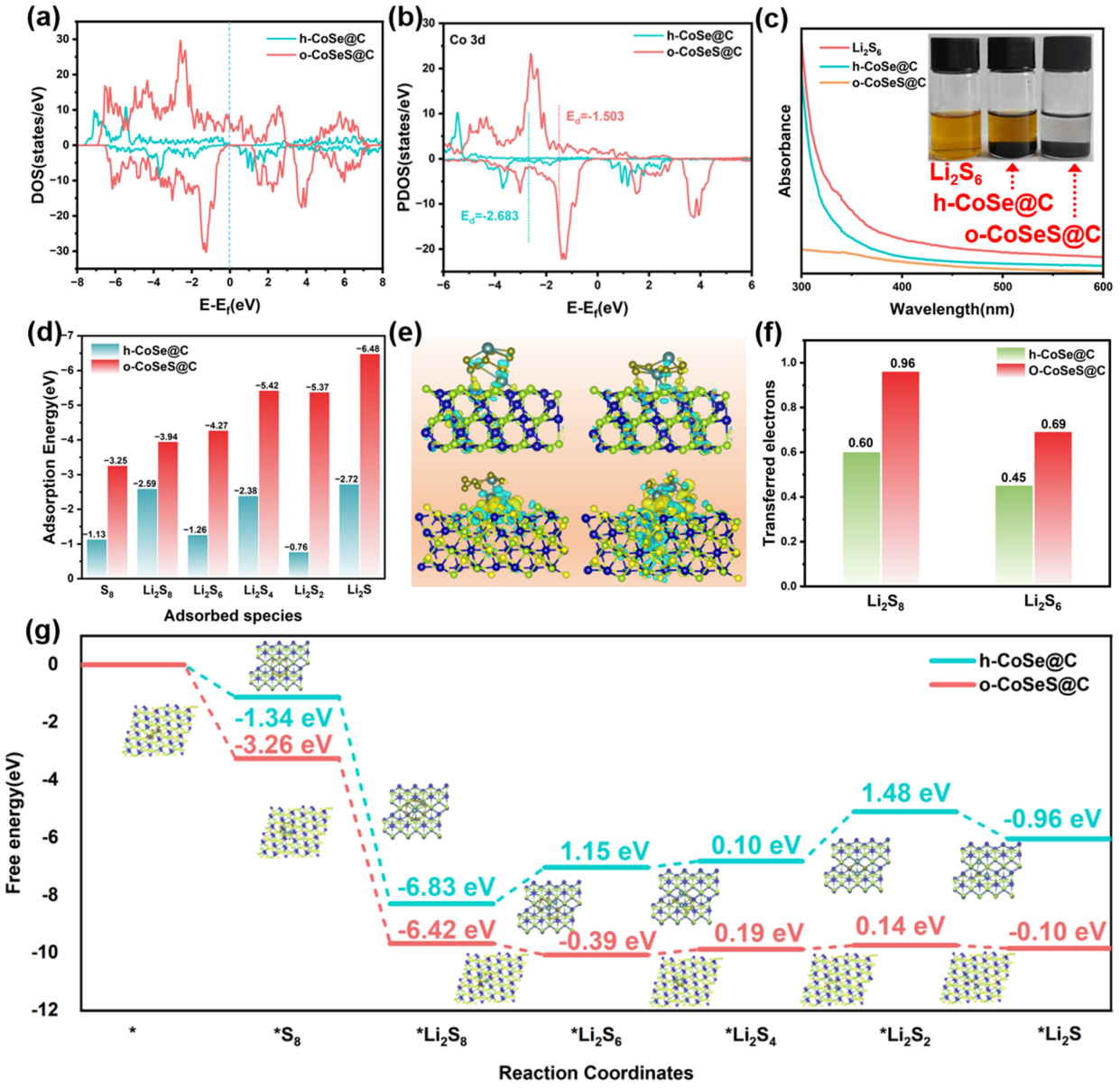


**Figure 6.** (a) Total density of states; (b) co-projected DOS of h-CoSe@C and o-CoSeS@C; (c) optical images and UV−vis spectra of $Li_2S_6$ adsorption on both materials; (d) adsorption energies of various polysulfides; (e) differential charge density maps for $Li_2S_8$ and $Li_2S_6$ adsorption (yellow: charge accumulation, green: charge depletion); (f) corresponding Bader charge analysis; and (g) Gibbs free energy profiles for polysulfide reduction catalyzed by h-CoSe@C and o-CoSeS@C.

structure. Figure 6a shows that o-CoSeS@C possessed a higher DOS around the Fermi level, indicating that sulfur doping provided additional electronic states. These states facilitated electron exchange with LiPSs, thereby markedly enhancing the adsorption capacity and catalytic performance. Moreover, the phase transition induced by sulfur doping caused a significant change from a low spin state to a high spin one of the active Co centers, which enhanced its catalytic activity. A comprehensive investigation of the projected density of states (PDOS) of Co was conducted to examine the effects of this change. Figure 6b shows that the Co peak in o-CoSeS@C was closer to the Fermi level, suggesting that its d-orbital electrons were more accessible for electron conduction and chemical reactions. Furthermore, the d-band center was a critical factor that influences the catalytic activity of transition metals, thereby reinforcing this tendency. The d-band center of Co in o-CoSeS@C was −1.503 eV, whereas that in h-CoSe@C was−2.683 eV. The proximity of the d-band center to the Fermi level in o-CoSeS@C indicated that the Co atoms in this material had a reduced binding energy, which was advantageous for catalytic processes. Subsequently, the d orbital splitting of Co ($d_{x^2-y^2}$, $d_{z^2}$, $d_{xy}$, $d_{yz}$, and $d_{xz}$) was analyzed before and after the phase shift induced by sulfur doping. The DOS of the Co d orbitals in h-CoSe@C shifted closer to the Fermi level following LiPSs adsorption (Figure S19a, Supporting Information). Conversely, for o-CoSeS@C, the DOS deviated from the Fermi level (Figure S19b, Supporting Information). According to the d-band theory, the position of the d-band relative to the Fermi level is crucial for adsorbate-metal interactions. Upon interaction with the catalyst, the valence electrons of the LiPSs interact with the d electrons, forming bonding and antibonding states. The displacement of the Co d orbitals from the Fermi level reduces the d DOS at that location, improving the bonding and capacity for LiPS


https://doi.org/10.1021/acsami.5c19431
ACS Appl. Mater. Interfaces 2026, 18, 4779−4791

adsorption. If the d orbitals move closer to the Fermi level, then the adsorption strength diminishes. The interaction between the Co d orbitals and LiPSs in o-CoSeS@C was stronger than that in h-CoSe@C, indicating an enhanced adsorption capacity and confirming that sulfur doping improved the catalytic performance of the material. Visual adsorption tests were performed to further examine the LiPS adsorption capabilities of h-CoSe@C and o-CoSeS@C. To further elucidate the relationship between the Co spin state and catalytic kinetics, we performed spin density and projected charge density analyses. The results reveal that high-spin Co in CoSeS exhibits uniform spin distribution, a moderate d-band center shift, and continuous Co−S orbital hybridization during the stepwise LiPS conversion ($Li_2S_4 \rightarrow Li_2S_2 \rightarrow Li_2S$), thereby substantially lowering the activation barriers. In contrast, low-spin Co in CoSe shows localized spin density, a pronounced upward shift of the d-band center, and reduced orbital overlap due to electron filling in antibonding states, which kinetically hinders the conversion process. This mechanism aligns consistently with the experimental CV/GITT results, where CoSeS-based cells display smaller polarization and faster redox kinetics, directly corroborating that the high-spin Co-modulated electronic structure is key to enabling efficient LiPS conversion (Figure S20). Figure 6c shows optical images of equivalent masses of h-CoSe@C and o-CoSeS@C immersed in a $Li_2S_6$ solution with an identical concentration for 2 h. This comparison indicated that the $Li_2S_6$ solution in the control group remained unchanged. However, the solution with h-CoSe@C exhibited a mild yellow shade, whereas the solution with o-CoSeS@C became nearly transparent. UV−vis analysis was conducted on the supernatant after the centrifugation of each sample. The o-CoSeS@C sample exhibited the lowest absorption intensity peak, indicating the highest LiPS adsorption capability. These observations demonstrated that o-CoSeS@C exhibited a significantly enhanced adsorption capability of LiPSs. Furthermore, Figure 6d shows that o-CoSeS@C consistently displayed higher adsorption energies for various sulfur species, which aligned well with the experimental observations. The electron gain, loss, and transfer behaviors of h-CoSe@C and o-CoSeS@C were further comprehensively examined by using differential charge density maps. As shown in Figure 6e, o-CoSeS@C exhibited greater electron accumulation at the interface between its active sites and $Li_2S_8$ and $Li_2S_6$ compared with h-CoSe@C, confirming a stronger interaction between LiPSs and their active sites. Figure 6f illustrates the electron transport between the catalyst active sites and LiPSs during the reaction. The active sites of o-CoSeS@C transmitted 0.96 eV of electrons to $Li_2S_8$ and 0.69 eV to $Li_2S_6$, both of which were higher than the corresponding values of 0.6 and 0.45 eV for h-CoSe@C. These results indicated that sulfur doping optimized the electronic structure of o-CoSe@C, enhancing its transfer capability of the electron during LiPS adsorption and catalysis, thereby significantly improving its electrochemical performance. To investigate the interaction mechanism between the h-CoSe@C and o-CoSeS@C catalysts and LiPSs, DFT calculations were conducted to analyze variations of the Gibbs free energy throughout the LiPS conversion process ($S_8 \rightarrow Li_2S_8 \rightarrow Li_2S_6 \rightarrow Li_2S_4 \rightarrow Li_2S_2 \rightarrow Li_2S$). Figure 6g shows that the o-CoSeS@C catalyst could spontaneously transform $S_8$ to $Li_2S_6$, and $Li_2S_2$ to $Li_2S$, whereas the h-CoSe@C catalyst exhibited spontaneity only during the conversions from $S_8$ to $Li_2S_8$ and from $Li_2S_2$ to $Li_2S$. The energy barriers in the critical reaction stages of h-CoSe@C were significantly higher than those of o-CoSeS@C. During the pivotal transition from liquid-soluble $Li_2S_4$ to solid-insoluble $Li_2S_2$ and $Li_2S$, the o-CoSeS@C catalyst exhibited Gibbs free energy changes of 0.14 and 0.1 eV, respectively, which were significantly lower than the 1.48 and 0.96 eV observed for h-CoSe@C. The results indicated that sulfur doping optimized the electronic structure, reduced the energy barriers in the polysulfide conversion process, and enhanced the kinetic feasibility of the phase transition stages, thereby improving the catalytic performance of o-CoSeS@C.

## 4. CONCLUSIONS

This study proposed a new catalyst strategy for Li−S batteries based on a biomimetic structural design and sulfur-doping-induced phase transformation. By employing a BC template combined with an EDTA-assisted method, we successfully constructed a hexagonal phase h-CoSe@C separator modification material featuring root-nodule morphology. This biomimetic design significantly enhanced the battery's electrochemical performance, achieving a discharge capacity of 1301 mAh $g^{-1}$. Further optimization was achieved through sulfur doping, which induced a phase transformation from hexagonal to orthorhombic cobalt selenide. This transformation facilitated the transition of cobalt atoms from low-spin to high-spin states, thereby enhancing the catalyst's adsorption capacity and catalytic conversion efficiency for LiPSs. DFT calculations provided mechanistic insights into the strong adsorption and efficient conversion of LiPSs by high-spin cobalt atoms, offering a theoretical foundation for catalyst design. The optimized catalyst (o-CoSeS@C) demonstrated exceptional performance with the Li−S battery, achieving an initial discharge capacity of 1509 mAh $g^{-1}$ at 0.1 C and a capacity decay rate of only 0.057% per cycle after 1000 cycles at 1 C. These results highlighted the excellent cycling stability and electrochemical performance of the developed catalyst, paving the way for advanced Li−S battery applications.

## ■ ASSOCIATED CONTENT

### Supporting Information

The Supporting Information is available free of charge at https://pubs.acs.org/doi/10.1021/acsami.5c19431.

Theoretical calculation details; high resolution spectra of Se 3d and S 2p; discussion of wettability results; lithium-ion diffusion coefficient calculation; and supporting figures (PDF)

## ■ AUTHOR INFORMATION


### Corresponding Author

**Zhihao Bao** − *Shanghai Key Laboratory of Special Artificial Microstructure Materials and Technology, School of Physics Science and Engineering, Tongji University, Shanghai 200092, China;* orcid.org/0000-0002-8708-7510; Email: zbao@tongji.edu.cn

### Authors

**Wei Yan** − *Shanghai Key Laboratory of Special Artificial Microstructure Materials and Technology, School of Physics Science and Engineering, Tongji University, Shanghai 200092, China*




https://doi.org/10.1021/acsami.5c19431
ACS Appl. Mater. Interfaces 2026, 18, 4779−4791

**Jun Chen** − *State Key Laboratory of Catalysis, Dalian Institute of Chemical Physics, Chinese Academy of Sciences, Dalian 116023, China*

**Abdul Mateen** − *Shanghai Key Laboratory of Special Artificial Microstructure Materials and Technology, School of Physics Science and Engineering, Tongji University, Shanghai 200092, China*

**Lin bin Tang** − *Shanghai Key Laboratory of Chemical Assessment and Sustainability, School of Chemical Science and Engineering, Tongji University, Shanghai 200092, China*

**Jiawen Li** − *Shanghai Key Laboratory of Special Artificial Microstructure Materials and Technology, School of Physics Science and Engineering, Tongji University, Shanghai 200092, China*

**Guoxiang Chen** − *Yiwu Research Institute of Fudan University, Yiwu 322000 Zhejiang, China*

**Yongfeng Mei** − *Yiwu Research Institute of Fudan University, Yiwu 322000 Zhejiang, China; Department of Materials Science and International Institute of Intelligent Nanorobots and Nanosystems, State Key Laboratory of Surface Physics, Fudan University, Shanghai 200438, China;* orcid.org/0000-0002-3314-6108

Complete contact information is available at: https://pubs.acs.org/10.1021/acsami.5c19431

### Author Contributions

#W.Y., J.C., and A.M. contributed equally to the work.

### Notes

The authors declare no competing financial interest.

## ■ ACKNOWLEDGMENTS

This work was supported by the research fund from Shanghai Key Laboratory of Special Artificial Microstructure Materials and Technology.

## ■ REFERENCES

(1) Qiu, C.; Li, A.; Qiu, D.; Wu, Y.; Jiang, Z.; Zhang, J.; Xiao, J.; Yuan, R.; Jiang, Z.; Liu, X.; Chen, X.; Song, H. One-Step Construction of Closed Pores Enabling High Plateau Capacity Hard Carbon Anodes for Sodium-Ion Batteries: Closed-Pore Formation and Energy Storage Mechanisms. *ACS Nano* **2024**, *18* (18), 11941−11954.

(2) Su, L.-L.; Wu, M.-X.; Sun, S.-Y.; Bi, C.-X.; Zheng, Z.; Zhao, M.; Li, B.-Q.; Zhang, X.-Q.; Huang, J.-Q. Long-Cycling Lithium−Sulfur Batteries Enabled by Reactivating Inactive Lithium. *ACS Energy Letters* **2025**, *10* (1), 313−319.

(3) Hua, W.; Shang, T.; Li, H.; Sun, Y.; Guo, Y.; Xia, J.; Geng, C.; Hu, Z.; Peng, L.; Han, Z.; Zhang, C.; Lv, W.; Wan, Y. Optimizing the p charge of S in p-block metal sulfides for sulfur reduction electrocatalysis. *Nature Catalysis* **2023**, *6* (2), 174−184.

(4) Chen, K.; Zhu, Y.; Huang, Z.; Han, B.; Xu, Q.; Fang, X.; Xu, J. J. A. Strengthened d−p orbital hybridization on metastable cubic Mo2C for highly stable lithium−sulfur batteries. *ACS Nano* **2024**, *18* (51), 34791−34802.

(5) Liu, Y.; Zhao, M.; Hou, L.-P.; Li, Z.; Bi, C.-X.; Chen, Z.-X.; Cheng, Q.; Zhang, X.-Q.; Li, B.-Q.; Kaskel, S.; Huang, J.-Q. An Organodiselenide Comediator to Facilitate Sulfur Redox Kinetics in Lithium−Sulfur Batteries with Encapsulating Lithium Polysulfide Electrolyte. *Angew. Chem., Int. Ed.* **2023**, *62* (30), No. e202303363.

(6) Jin, W.; Guo, Y.; Gan, T.; Shen, Z.; Zhu, X.; Zhang, P.; Zhao, Y. Cooperation of Multifunctional Redox Mediator and Separator Modification to Enhance Li-S Batteries Performance under Low Electrolyte/Sulfur Ratios. *Angew. Chem., Int. Ed.* **2024**, *64*, No. e202420544.

(7) Zhou, L.; Danilov, D. L.; Qiao, F.; Wang, J.; Li, H.; Eichel, R.-A.; Notten, P. H. L. Sulfur Reduction Reaction in Lithium−Sulfur Batteries: Mechanisms, Catalysts, and Characterization. *Adv. Energy Mater.* **2022**, *12* (44), No. 2202094.

(8) Shao, W.; Shi, H.; Jian, X.; Wu, Z.-S.; Hu, F. Hard-carbon anodes for sodium-ion batteries: recent status and challenging perspectives. *Adv. Energy Sustainability Res.* **2022**, *3* (7), No. 2200009.

(9) Razaq, R.; Din, M. M. U.; Småbråten, D. R.; Eyupoglu, V.; Janakiram, S.; Sunde, T. O.; Allahgoli, N.; Rettenwander, D.; Deng, L. Synergistic Effect of Bimetallic MOF Modified Separator for Long Cycle Life Lithium-Sulfur Batteries. *Adv. Energy Mater.* **2024**, *14* (3), No. 2302897.

(10) Chen, K.; Zhang, Y.; Fan, Z.; Zhu, J.; Xu, Q.; Xu, J. Valence Electronic Modulation Induced by Reinforcing Interfacial Coupling for Expediting Sulfur Redox in Li—S Batteries. *Adv. Funct. Mater.* **2025**, *35*, No. 2500574.

(11) Long, J.-J.; Yu, H.; Liu, W.-B. Structure engineering of cathode host materials for Li−S batteries. *Rare Metals* **2024**, *43* (4), 1370−1389.

(12) Leng, X.; Yang, K.; Sun, L.; Weng, J.; Xu, J. J. A. C. Modulating the Band Structure of Two-Dimensional Black Phosphorus via Electronic Effects of Organic Functional Groups for Enhanced Hydrogen Production Activity. *Angew. Chem. Int. Ed.* **2025**, *137* (5), No. e202416992.

(13) Qi, C.; Zu, S.; Zhu, X.; Zhang, T.; Li, L.; Song, L.; Jin, Y.; Zhang, M. Bamboo-shaped Co@NCNTs as superior sulfur host for Li-S batteries. *Appl. Surf. Sci.* **2022**, *601*, No. 154245.

(14) Deng, S.; Shi, X.; Zhao, Y.; Wang, C.; Wu, J.; Yao, X. Catalytic Mo2C decorated N-doped honeycomb-like carbon network for high stable lithium-sulfur batteries. *Chemical Engineering Journal* **2022**, *433*, No. 133683.

(15) Ai, G.; Dai, Y.; Mao, W.; Zhao, H.; Fu, Y.; Song, X.; En, Y.; Battaglia, V. S.; Srinivasan, V.; Liu, G. Biomimetic Ant-Nest Electrode Structures for High Sulfur Ratio Lithium−Sulfur Batteries. *Nano Lett.* **2016**, *16* (9), 5365−5372.

(16) Shi, G.; Shi, X.; Hou, Y.; Zhang, S.; Han, Y.; Li, Q. An ant-nest like hierarchical nanoreactor for highly efficient sulfur species redox reactions. *J. Alloys Compd.* **2022**, *914*, No. 165211.

(17) Yao, Y.; Chang, C.; Sun, H.; Guo, D.; Li, R.; Pu, X.; Zhai, J. Hollow Ni3Se4 with High Tap Density as a Carbon-Free Sulfur Immobilizer to Realize High Volumetric and Gravimetric Capacity for Lithium−Sulfur Batteries. *ACS Appl. Mater. Interfaces* **2022**, *14* (22), 25267−25277.

(18) Cui, J.; Liu, J.; Chen, X.; Meng, J.; Wei, S.; Wu, T.; Wang, Y.; Xie, Y.; Lu, C.; Zhang, X. Ganoderma Lucidum-derived erythrocyte-like sustainable materials. *Carbon* **2022**, *196*, 70−77.

(19) Gopiraman, M.; Jatoi, A. W.; Hiromichi, S.; Yamaguchi, K.; Jeon, H.-Y.; Chung, I.-M.; Ick Soo, K. Silver coated anionic cellulose nanofiber composites for an efficient antimicrobial activity. *Carbohydr. Polym.* **2016**, *149*, 51−59.

(20) Zhao, J.; Quan, X.; Chen, S.; Liu, Y.; Yu, H. Cobalt Nanoparticles Encapsulated in Porous Carbons Derived from Core−Shell ZIF67@ZIF8 as Efficient Electrocatalysts for Oxygen Evolution Reaction. *ACS Appl. Mater. Interfaces* **2017**, *9* (34), 28685−28694.

(21) Kim, Y. B.; Kim, T. H.; Kim, S.; Jeong, S.; Chan Kang, Y.; Lee, D.; Park, G. D. Multiple heteroatom-doped cobalt sulfoselenide@C yolk-shell microsphere as excellent anode materials for sodium-ion batteries and their conversion reaction mechanism with sodium ions. *J. Power Sources* **2024**, *618*, No. 235186.

(22) Park, S.-K.; Kim, J. K.; Kang, Y. C. Excellent sodium-ion storage performances of CoSe2 nanoparticles embedded within N-doped porous graphitic carbon nanocube/carbon nanotube composite. *Chemical Engineering Journal* **2017**, *328*, 546−555.

(23) Chen, Q.; Liang, Q.; He, S.-A.; Cui, Z.; Liu, Q.; Zhu, J.; Zou, R. Co0.85Se particles encapsulated in the inner wall of nitrogen-doped carbon matrix nanotubes with rational interfacial bonds for high-performance lithium-ion batteries. *Dalton Transactions* **2021**, *50* (33), 11458−11465.

(24) Zhao, C.; Huo, F.; Yang, Y.; Ruan, J.; Chai, F.; Xu, H.; Liu, Y.; Zhang, L.; Cabot, A.; Sun, Z.; Zhang, Y. Development of Synergistically Efficient Ni−Co Pair Catalytic Sites for Enhanced Polysulfide Conversion in Lithium−Sulfur Batteries. *Adv. Funct. Mater.* **2024**, *34* (37), No. 2402175.
(25) Xiao, H.; Li, K.; Zhang, T.; Liang, X.; Zhang, F.; Zhuang, H.; Zheng, L.; Gao, Q. High loading atomically distributed Fe asymmetrically coordinated with pyridinic and pyrrolic N on porous N-rich carbon matrix driving high performance of Li-S battery. *Chemical Engineering Journal* **2023**, *471*, No. 144553.
(26) Wang, C.; Zhang, B.; Xia, H.; Cao, L.; Luo, B.; Fan, X.; Zhang, J.; Ou, X. Composition and Architecture Design of Double-Shelled Co0.85Se1−S@Carbon/Graphene Hollow Polyhedron with Superior Alkali (Li, Na, K)-Ion Storage. *Small* **2020**, *16* (17), No. 1905853.
(27) Kim, A.; Oh, S. H.; Adhikari, A.; Sathe, B. R.; Kumar, S.; Patel, R. Recent advances in modified commercial separators for lithium−sulfur batteries. *Journal of Materials Chemistry A* **2023**, *11* (15), 7833−7866.
(28) Waqas, M.; Niu, Y.; Tang, M.; Pang, Y.; Ali, S.; Dong, Y.; Lv, W.; He, W. A decade of development in cathode-facing surface modified separators for high-performance Li-S batteries. *Energy Storage Materials* **2024**, *72*, No. 103682.
(29) Wu, Z.; Chen, S.; Wang, L.; Deng, Q.; Zeng, Z.; Wang, J.; Deng, S. Implanting nickel and cobalt phosphide into well-defined carbon nanocages: A synergistic adsorption-electrocatalysis separator mediator for durable high-power Li-S batteries. *Energy Storage Materials* **2021**, *38*, 381−388.
(30) Dong, C.; Zhou, C.; Wu, M.; Yu, Y.; Yu, K.; Yan, K.; Shen, C.; Gu, J.; Yan, M.; Sun, C.; Mai, L.; Xu, X. Boosting Bi-Directional Redox of Sulfur with Dual Metal Single Atom Pairs in Carbon Spheres Toward High-Rate and Long-Cycling Lithium−Sulfur Battery. *Adv. Energy Mater.* **2023**, *13* (30), No. 2301505.
(31) Cheng, Z.; Chen, Y.; Lian, J.; Chen, X.; Xiang, S.; Chen, B.; Zhang, Z. Interface Engineering of MOF Nanosheets for Accelerated Redox Kinetics in Lithium-Sulfur Batteries. *Angew. Chem., Int. Ed.* **2024**, *137*, No. e202421726.
(32) Ye, X.; Wu, F.; Xue, Z.; Yuan, H.; Mei, S.; Wang, J.; Yang, R.; Wu, X.; Zhao, X.; Pan, H.; Zhang, Q.; Xiang, Y.; Huang, M.; Li, F. Accelerated Polysulfide Conversion by Rationally Designed NiS2-CoS2 Heterostructure in Lithium−Sulfur Batteries. *Adv. Funct. Mater.* **2024**, *35*, No. 2417776.
(33) Zhang, X.; Lv, X.; Du, X.; Qi, M.; Mao, S.; Wang, Y. High-Temperature-Mediated Assembly of Polyoxometalate-Induced Ordered Carbonaceous Superstructures. *Angew. Chem., Int. Ed.* **2024**, *137*, No. e202423242.
(34) Yu, J.-H.; Lee, B.-J.; Zhou, S.; Sung, J. H.; Zhao, C.; Shin, C.-H.; Yu, B.; Xu, G.-L.; Amine, K.; Yu, J.-S. Tailoring-Orientated Deposition of Li2S for Extreme Fast-Charging Lithium−Sulfur Batteries. *ACS Nano* **2024**, *18* (46), 31974−31986.
(35) Chen, S.; Luo, J.; Li, N.; Han, X.; Wang, J.; Deng, Q.; Zeng, Z.; Deng, S. Multifunctional LDH/Co9S8 heterostructure nanocages as high-performance lithium−sulfur battery cathodes with ultralong lifespan. *Energy Storage Materials* **2020**, *30*, 187−195.
(36) Wu, X.; Liu, N.; Wang, M.; Qiu, Y.; Guan, B.; Tian, D.; Guo, Z.; Fan, L.; Zhang, N. A Class of Catalysts of BiOX (X = Cl, Br, I) for Anchoring Polysulfides and Accelerating Redox Reaction in Lithium Sulfur Batteries. *ACS Nano* **2019**, *13* (11), 13109−13115.
(37) Li, H.; Chuai, M.; Xiao, X.; Jia, Y.; Chen, B.; Li, C.; Piao, Z.; Lao, Z.; Zhang, M.; Gao, R.; Zhang, B.; Han, Z.; Yang, J.; Zhou, G. Regulating the Spin State Configuration in Bimetallic Phosphorus Trisulfides for Promoting Sulfur Redox Kinetics. *J. Am. Chem. Soc.* **2023**, *145* (41), 22516−22526.
(38) Lai, T.; Bhargav, A.; Manthiram, A. Lithium Tritelluride as an Electrolyte Additive for Stabilizing Lithium Deposition and Enhancing Sulfur Utilization in Anode-Free Lithium−Sulfur Batteries. *Adv. Funct. Mater.* **2023**, *33* (43), No. 2304568.
(39) Wang, B.; Wang, L.; Kong, Y.; Wang, F.; Jing, Z.; Yang, X.; Qian, Y.; Chen, M.; Xu, L. Hafnium Diboride Spherical Superstructure Born of 5d-Metal Hf-MOF-Induced p Orbital Activity of B Atom and Enhanced Kinetics of Sulfur Cathode Reaction. *Adv. Energy Mater.* **2023**, *13* (22), No. 2300590.
(40) Zhao, M.; Tan, P.; Cai, D.; Liu, Y.; Zhang, C.; Fei, B.; Sa, B.; Chen, Q.; Zhan, H. Customizing Component Regulated Dense Heterointerfaces for Crafting Robust Lithium-Sulfur Batteries. *Adv. Funct. Mater.* **2023**, *33* (8), No. 2211505.
(41) Chen, K.; Zhang, G.; Xiao, L.; Li, P.; Li, W.; Xu, Q.; Xu, J. Polyaniline Encapsulated Amorphous V2O5 Nanowire-Modified Multi-Functional Separators for Lithium−Sulfur Batteries. *Small Methods* **2021**, *5* (3), No. 2001056.
(42) Li, H.; Huang, Z.; Qian, P.; Wang, Y.; Gao, R.; Bendounan, A.; Wang, H.; Chen, Z.; Zeng, H.; Li, G. Phosphorus-Tuned Nickel Boride Nanocatalyst with Enhanced p−p Interaction for Expediting Sulfur Electrochemistry in Lithium-Sulfur Batteries. *Adv. Funct. Mater.* **2024**, *35*, No. 2419837.
(43) Chen, Q.; Li, T.; Huang, H.; Wang, W.; Yu, Z.; Liu, Q.; Liu, L. Pyridinic-N-rich single-atom vanadium catalysts boost conversion kinetics of polysulfides for high performance lithium-sulfur batteries. *Nano Energy* **2025**, *133*, No. 110509.
(44) Zhou, X.; Mao, W.; Ye, C.; Liang, Q.; Wang, P.; Wang, X.; Tang, S. Heteroatoms Synergistic Anchoring Vacancies in Phosphorus-Doped CoSe2 Enable Ultrahigh Activity and Stability in Li−S Batteries. *Nano-Micro Lett.* **2025**, *17* (1), 308.
(45) Hou, R.; Li, Y.; Wang, Z.; Shi, Z.; Li, N.; Miao, F.; Shao, G.; Zhang, P. In Situ 1D Carbon Chain-Mail Catalyst Assembly for Stable Lithium−Sulfur Full Batteries. *Small* **2023**, *19* (35), No. 2300868.
(46) Han, F.; Yan, D.; Guan, X.; Lu, Q.; Yin, S.; Yan, Y.; Zhou, H.; Yang, P.; Zhang, Q.; Zhang, S. Self-assembled 3D CoSe-based sulfur host enables high-efficient and durable electrocatalytic conversion of polysulfides for flexible lithium-sulfur batteries. *Energy Storage Mater.* **2024**, *71*, No. 103652.
(47) Selabi, N. B. S.; Zhou, Y.; Che, L.; Liu, M.; Mo, L.; Tian, X. Optimizing polysulfides adsorption and conversion via crystal-strain modulation for performance-enhanced Li-S batteries. *Chem. Eng. J.* **2025**, *504*, No. 157724.




https://doi.org/10.1021/acsami.5c19431
ACS Appl. Mater. Interfaces 2026, 18, 4779−4791